On the Synchronization of Uncoupled Multistatic PMCW Radars

David Werbunat[ID], *Graduate Student Member, IEEE*, Julian Aguilar[ID], *Graduate Student Member, IEEE*, Mohanid Almarashly, Vinzenz Janoudi[ID], *Graduate Student Member, IEEE*, Simon Stephany, Daniel Gil Gaviria[ID], *Graduate Student Member, IEEE*, Ahmet Çağrı Ulusoy[ID], *Member, IEEE*, and Christian Waldschmidt[ID], *Fellow, IEEE*

Abstract— Radar networks and multistatic synthetic aperture radars (SARs) allow overcoming the limitations of single radar sensors. However, a good synchronization of the radar sensors is crucial to avoid performance loss due to phase noise and frequency offsets. While this is usually done via cables or dedicated synchronization signals, digital radars allow for new techniques. This work proposes a new concept for the synchronization of phase-modulated continuous wave (PMCW) radars. The synchronization is performed solely by digital signal processing on the receiver side, adapting techniques known from digital communications. It mitigates effects caused by incoherency, which are phase noise, carrier frequency offsets and phase deviations of the local oscillator (LO), and sampling frequency offsets. At first, the impact of these effects is mathematically derived and analyzed in detail. Then, the proposed synchronization concept is presented, and its performance is thoroughly evaluated. Very good results are obtained not only in simulations but also in measurements with a 77-GHz radar demonstrator.

Index Terms— Bistatic, carrier frequency offset (CFO), carrier recovery, digital radar, multistatic, phase noise, phase-modulated continuous wave (PMCW) radar, pseudo noise (PN) radar, pseudorandom binary sequence (PRBS) radar, pseudorandom noise (PRN) radar, radar network, sample frequency offset (SFO), sample rate offset, synchronization, timing recovery.

I. INTRODUCTION

WITH more and more applications in automotive [1], industry [2], and remote sensing [3], and favored by the progress in radio frequency (RF) chip design [4], [5] and digital RF systems [6], [7], the use of radar sensors is increasing rapidly [1]. To enhance performance beyond the limits of a single radar, the next step is to combine multiple radar sensors to form a so-called radar network [8], [9]. However, the full potential of a radar network can only be exploited if the sensors are synchronized to enable bi- or multistatic signal evaluation [9], [10]. This allows one radar to evaluate the signal from another radar within the network without the performance being affected by effects like uncorrelated phase noise. By this way, a radar network can enable multistatic synthetic aperture radar (SAR) [8], [10], [11], [12] as well as network-based direction of arrival (DoA) estimation [9], [13], [14].

Different synchronization strategies have been proposed for radar networks. Low-frequency coupling using cables [14], [15] and the use of a separate synchronization signal [16], [17] are among the most typical variants. Alternatively, the necessity of synchronization can be avoided by using costly high-quality signal sources with a very low phase noise [18], [19]. However, all these approaches lack the flexibility and simplicity of plain uncoupled radar sensors.

The issue of synchronizing RF systems is, however, well-known in digital communications. Communication systems are inherently uncoupled, and typically, the synchronization is performed at the receiver (Rx) only. There are various synchronization techniques used in communication systems [20], [21], [22], with a thorough literature overview being given in [22]. These approaches include methods for the timing recovery, i.e., the recovery of a sample frequency offset (SFO) between the digital-to-analog converter (DAC) and the analog-to-digital converter (ADC) [23], [24], [25], as well as carrier synchronization methods. Often, pilot tones or pilot sequences are used for the synchronization of multicarrier signals [21], [26] as well as single-carrier signals [27], [28], [29]. However, for single-carrier signals modulated with binary phase-shift keying (BPSK) and *M*PSK, phase-locked loops (PLLs) can be used by implementing Costas loops [30], [31] or squaring loops [32]. These PLL-based methods provide carrier synchronization that includes not only frequency offset mitigation but also phase noise mitigation. While they were developed for analog signal processing, they can also be implemented digitally [33], [34].

Similar to communication systems, digital radars sample signals at their full RF bandwidth (BW), allowing for highly flexible digital signal processing. Thus, they provide the opportunity to adapt carrier and timing recovery methods from communication systems. This is especially true for phase-modulated continuous wave (PMCW) radars. These radars use BPSK modulation combined with a correlation-based signal evaluation [35], [36], [37]. Hence,

carrier recovery methods known from BPSK-modulated communication signals have the potential to successfully synchronize them. However, to the best of the authors' knowledge, there are very few publications on synchronized PMCW radars. The proposed multistatic approaches use low-frequency carriers synchronized by global positioning system (GPS) [38] or show only basic simulations [39]. Therefore, the aim of this work is to present algorithms for Rx-side synchronization of uncoupled PMCW radars and to analyze their performance using extensive simulations and measurements at 77 GHz.

This work at first presents a detailed analysis of the effects caused due to incoherency when using uncoupled PMCW radars in networks for multistatic evaluation. Then, it proposes recovery methods to overcome these issues. Uncoupled means that there is no reference distribution, neither for the signal sources used to generate the carriers, in the following called local oscillators (LOs), nor for the sampling clock references of the DACs and ADCs. Hence, the effects examined include the phase noise and carrier frequency offset (CFO) caused by uncoupled LOs as well as errors caused by the SFO between the DAC and the ADC. As the trigger distribution is mainly seen as system-dependent, trigger errors are not investigated in this work. Furthermore, methods are proposed to correct the effects and thus provide a coherent signal evaluation by digital signal processing on the Rx side only. To mitigate CFO and phase noise, a carrier recovery is performed. This is possible by using a superheterodyne Rx, where the signal is sampled on the intermediate frequency (IF) carrier. Hence, the IF carrier including the transmitter (Tx) and receiver (Rx) phase noise can be recovered digitally using a squaring loop [32], before the recovered carrier is used for an in-phase and quadrature (IQ) down-conversion to baseband. Additionally, a timing recovery detecting the SFO is presented, and errors caused by unsynchronized DACs and ADCs are corrected. The goal of this article is to examine and evaluate the recovery methods in detail, thus providing a basis for further research regarding uncoupled PMCW radar networks. Thus, validation measurements are performed using a 77 GHz radar with a single Tx and Rx channel. The LO sources as well as the DAC and ADC can be used either with a low-frequency coupling or completely uncoupled, enabling a detailed examination of the errors caused by incoherency as well as the performance of the recovery methods.

This article is divided into three thematic parts. Part one includes a detailed investigation on how incoherency affects the radar signal evaluation in the case of uncoupled PMCW radars. For this purpose, at first, a signal model is introduced in Section II. It provides a basis for the detailed mathematical description of the effects of incoherency, which is presented in Section III and accompanied by simulations and measurements. In part two of this article, methods are proposed to correct those effects. Although in real scenarios they occur jointly, in this part, SFO due to uncoupled DAC/ADC and effects caused by uncoupled LOs are considered separately. This allows evaluating the proposed correction methods individually. A method for the SFO detection and correction is presented in Section IV, and in Section V, a carrier recovery is proposed to mitigate the influence of the uncoupled LOs. Both

are accompanied by a validation of the methods. Finally, in the last part of this article, the recovery methods are combined. Using an uncoupled radar setup, Section VI shows the ability to recover the receive signal and to generate a corrected range-Doppler (Rv) plot despite SFO, CFO, and phase noise.

II. SIGNAL MODEL

At first, the basic concept of a PMCW radar is briefly explained. This includes a detailed signal model of the resulting Rx signal for the coupled and uncoupled cases.

A. Transmit Signal

PMCW radars transmit a phase-coded baseband signal $m(t)$ mixed on a continuous wave (CW) RF carrier with the frequency f_{Tx} [36], leading to the transmit signal

$$x_{\text{Tx}}(t) = a_{\text{Tx}} m(t) s_{\text{Tx}}(t) \tag{1}$$

where a_{Tx} is the amplitude of the transmit signal and

$$s_{\text{Tx}}(t) = e^{j(2\pi f_{\text{Tx}} t + \phi_{\text{Tx}}(t))} \tag{2}$$

the Tx's LO signal. The time-dependent phase $\phi_{\text{Tx}}(t)$ is the phase offset of the LO including phase noise. The baseband signal $m(t)$ can be described using a pulse filter $h(t)$ and the BPSK code sequence of length L_c itself, represented as vector $\mathbf{c} \in \{-1, 1\}^{L_c}$ [40]. Repeating the same code sequence m_0 for N_s times leads to

$$m(t) = \sum_{p=0}^{N_s-1} m_0\ (t - pL_c T_c) = \sum_{p=0}^{N_s-1} \sum_{i=0}^{L_c-1} c[i] h\big(t - (i + pL_c)T_c\big) \tag{3}$$

where $c[i]$ corresponds to the ith element of $\mathbf{c}$. The duration of a single pulse is denoted as T_c, leading to a code rate of $R_c = 1/T_c$. As pulse function, typically, a rectangular pulse is used [36], [41], [42], [43].

B. Reference Link (RL)

For the carrier recovery proposed in Section V, it is crucial to have one signal path between Tx and Rx that results in a higher Rx power than the superposition of all other received signals. In the following, this signal path is referred to as reference link (RL) and denoted by index 0. Depending on the radar and network setup, there are different types of signal paths resulting in the RL. For Tx–Rx pairs close together, the RL may be caused by mutual coupling of the antennas. Being further apart, the RL refers to the line-of-sight (LoS) path.

C. Receive Signal

On Rx side, a superposition of signals is received via different paths. This includes the RL denoted as $k = 0$ and the reflections at all N_T targets denoted as $k = 1 \ldots N_T$. The downconverted Rx signal is described as

$$x_{\text{Rx}}(t) = \sum_{k=0}^{N_T} a_{\text{Rx},k} m(t - \tau_k) e^{j2\pi f_{\text{d},k} t} s_{\text{Tx}}(t - \tau_k) s_{\text{Rx}}(t) + n(t) \tag{4}$$

This article has been accepted for inclusion in a future issue of this journal. Content is final as presented, with the exception of pagination.

WERBUNAT et al.: ON SYNCHRONIZATION OF UNCOUPLED MULTISTATIC PMCW RADARS 3

with τ_k being the delay and $f_{d,k}$ the Doppler shift of the kth path. The thermal noise is represented by $n(t)$. For the down-conversion, an IQ mixer is used. The Rx carrier used for down-conversion is

$$s_{Rx}(t) = e^{-j(2\pi f_{Rx}t + \phi_{Rx}(t))}. \tag{5}$$

Hence, the result of the up- and down-conversion equals

$$s_{Tx}(t - \tau_k)s_{Rx}(t) = e^{j2\pi(f_{Tx}-f_{Rx})t}\, e^{-j2\pi f_{Tx}\tau_k}\, e^{j(\phi_{Tx}(t-\tau_k)-\phi_{Rx}(t))}. \tag{6}$$

In the next step, the coupled coherent case and the uncoupled case with an incoherent Rx signal are examined separately.

1) Coherent Rx Signal: In the case of a coupled Tx–Rx pair, the same LO is used on Tx and on Rx side, leading to $f_{Rx} = f_{Tx}$ and $\phi_{Rx}(t) = \phi_{Tx}(t)$, and thus to a coherent Rx signal. It holds that

$$s_{Tx}(t - \tau_k)s_{Rx}(t) = e^{-j2\pi f_{Tx}\tau_k}\, e^{j(\phi_{Tx}(t-\tau_k)-\phi_{Tx}(t))}. \tag{7}$$

Considering the range correlation effect [44], the phase noise, i.e. the term $e^{j(\phi_{Tx}(t-\tau_k)-\phi_{Tx}(t))}$ is neglectable for small ranges R. Therefore, only the target-induced range-dependent phase offset $\phi_{\tau,k} = -2\pi f_{Tx}\tau_k$ remains.

2) Incoherent Rx Signal: In the case of an uncoupled Tx–Rx pair, there are two independent LOs for Tx and Rx, and thus, $s_{Rx}(t) \neq s_{Tx}(t)$. This leads to an incoherent Rx signal. For simplification, the CFO

$$f_{cfo} = f_{Tx} - f_{Rx} \tag{8}$$

and the resulting phase error

$$\phi_n(t) = \phi_{Tx}(t - \tau_k) - \phi_{Rx}(t) \tag{9}$$

which includes phase noise that is introduced. The CFO is defined to be constant during a measurement frame, whereas $\phi_n(t)$ may also include a frequency drift within a frame. Combined with (6), this leads to

$$s_{Tx}(t - \tau_k)s_{Rx}(t) = e^{j2\pi f_{cfo}t}\, e^{-j2\pi f_{Tx}\tau_k}\, e^{j\phi_n(t)}. \tag{10}$$

Both f_{cfo} and $\phi_n(t)$ significantly affect the radar signal processing, which is explained in detail in Section III.

D. Signal Processing

As shown in Fig. 1, the processing of the Rv matrix is a three-step process. In the first step, the downconverted receive signal is reshaped to an $L_c \times N_s$ matrix. If the sampling rate is higher than the code rate, the matrix size is increased to $n_b L_c \times N_s$, where $n_b = f_s/R_c$. Every column includes the superposition of the single sequences shifted by different path delays τ_k as $\sum_{k=0}^{N_T} m_0(t - \tau_k)$. Performing a column-wise cross-correlation with the transmit sequence $m_0(t)$ in the next step, one gets a peak corresponding to the delays τ_k and thus the range of every target. It should be noted that for the correlation, $m_0(t)$ must be sampled with the same f_s.

In the last step, the Doppler frequency shift is evaluated. Due to the Doppler shift, there is a velocity-dependent phase rotation of

$$x_{\text{Doppler},k}[p] = e^{j2\pi f_{d,k}\frac{L_c}{R_c}p} \tag{11}$$
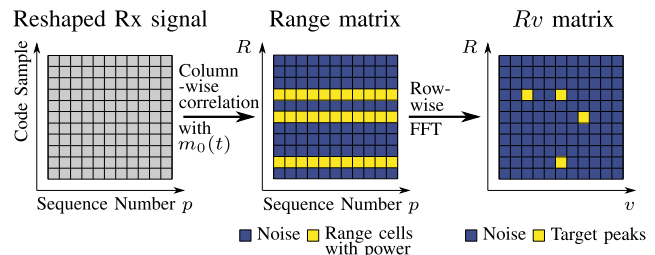

Fig. 1. Concept of the signal evaluation of a PMCW radar. The first matrix depicts the reshaped Rx signal, with the samples of one received code sequence in each column. The number of rows equals the number of samples per sequence $n_b \cdot L_c$, and the number of columns equals N_s. The range matrix is generated by correlating each column with the Tx code sequence $m_0(t)$. Each row with power equals the range cell of one or multiple targets, which is equivalent to a certain delay τ. With a row-wise FFT, the Doppler is evaluated, generating the Rv matrix.

TABLE I
RADAR PARAMETERS

Carrier frequency	f_c	77 GHz
Code rate	R_c	1 GHz
Code length	L_c	4008
Code type		APAS
Pulse function		rect
Code repetitions	N_s	256
Range resolution	ΔR	0.15 m
Velocity resolution	Δv	1.89 m/s
Unambiguous range	R_{ua}	300.4 m
Unambiguous velocity	v_{ua}	±242.9 m/s

versus the columns of the matrix. This phase rotation can now be evaluated by applying a row-wise fast Fourier transform (FFT), leading to a single peak per target in the corresponding bin of the resulting Rv matrix.

III. EFFECTS OF INCOHERENCY

In the next step, the influences of incoherency are examined in detail using simulations as well as measurements performed in an anechoic chamber. This not only includes errors due to uncoupled LOs, like CFO and phase noise, but also timing errors due to uncoupled DAC and ADC clocks.

A. Simulation Framework and Measurement Setup

The PMCW signal used in simulations and in measurements is coded with an almost perfect autocorrelation sequence (APAS) [45] of length $L_c = 4008$. It has a code rate of $R_c = 1$ GHz and is transmitted on a 77-GHz carrier. An overview over the PMCW parameters is given in Table I.

Simulations are performed using an equivalent complex baseband simulation framework. In the Tx and Rx, the signal is up- and downconverted on a simulated carrier. To save computational resources, the carrier is not at 77 GHz, but either a 1-GHz carrier, or, in the case of the simulations presented in Section V, the 1.1-GHz IF carrier. However, the channel, e.g., the Doppler frequency, is simulated to match a 77-GHz carrier frequency. The simulations are performed using a sample rate of 5 GHz to fulfill the Nyquist criterion.

For measurements, the same setup is used as described in Section VI. However, in contrast to the measurements in
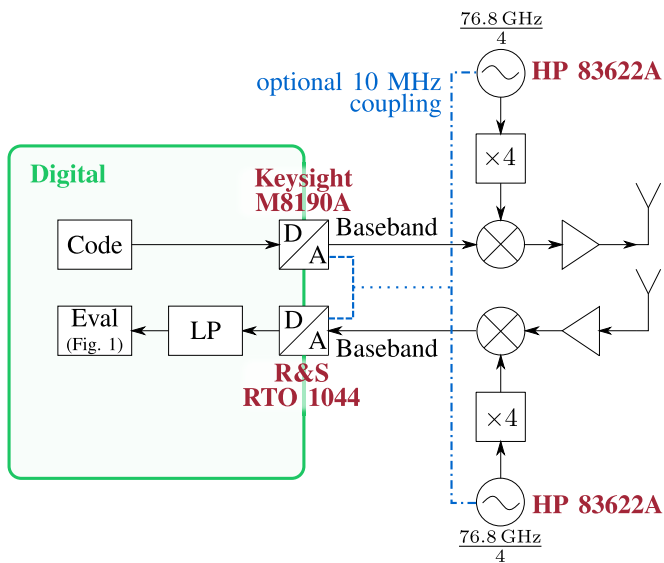
Fig. 2.   PMCW radar and digital signal processing without recovery steps.

Section VI, in this section, the signal is directly downconverted and sampled at baseband, equaling a standard PMCW radar setup. A block diagram is shown in Fig. 2. Two signal generators (HP 83622A) are used as LO for carrier generation. A Keysight M8190A arbitrary waveform generator (AWG) is used as DAC. The chosen Tx sample frequency is 1 GHz and equals R_c. As ADC, a Rohde & Schwarz RTO 1044 oscilloscope is used. Both the signal generators and the DAC/ADC can be coupled flexibly using a 10-MHz reference clock. This makes it possible to examine the influences of uncoupled LOs and uncoupled DAC/ADC separately. A drawback of this setup are the mixers, which are double-sideband (DSB) mixers. When used in direct down-conversion mode like in this section, it is not possible to distinguish positive and negative Doppler frequencies or frequency offsets.

Although the sampling frequencies of the DAC and ADC differ from each other, each is chosen to be usable for all measurements. On Tx side, the DAC is used with a sampling frequency of 1 GHz, corresponding to the code rate R_c. On Rx side, the signal is sampled either in baseband or, when performing the carrier recovery presented in Section V, on a 1.1-GHz IF carrier. In the latter case, a sampling frequency of at least 5 GHz is required for the ADC to satisfy the Nyquist criterion with back-off. However, due to the lack of an appropriate anti-aliasing low-pass filter (LP), a higher sampling frequency of 10 GHz is chosen for Rx, which is used in all measurements.

B. Carrier Frequency Offset

When comparing (4) and (10), it becomes apparent that a CFO, which is a frequency offset between the LOs, is evaluated in the same way as a Doppler shift. Hence, all targets additionally are shifted by the CFO f_{cfo}, leading to a velocity error of

$$v_{err} = \frac{1}{2} \frac{f_{cfo}}{f_{Tx}} c_0 \tag{12}$$

where c_0 is the speed of light. For a CFO larger than the unambiguous Doppler shift, i.e., $v_{err} \geq v_{ua}$, the targets are

cyclically shifted back into the Rv matrix. In the same manner as the Doppler shift, f_{cfo} also affects the range correlation. For the relationship between the Doppler shift and the reduction of the range correlation performance, it is referred to [46].

C. Phase Noise

For coupled Tx–Rx pairs, the influence of range-correlated phase noise has been researched [47]. For uncoupled Tx–Rx pairs, however, the impact of the, in this case, uncorrelated phase noise is much more severe.

There are two effects induced by phase noise. On the one hand, phase noise reduces the correlation properties of the binary code. This introduces evenly distributed sidelobes after the cross-correlation (range matrix in Fig. 1) which then are spread over the Doppler bins by the Doppler fast Fourier transform (FFT). This behavior increases the noise floor in the same manner as white Gaussian noise [47]. In this article, this effect is evaluated based on the peak-to-noise ratio (PNR). The PNR is calculated as the ratio between the peak power and the power of the maximum of the histogram of all Rv cells. This maximum corresponds to the mean power of the noise floor, assuming a normal distribution.

On the other hand, the uncorrelated phase noise introduces a skirt in the Doppler domain. With the Doppler FFT, the spectrum of the receive signal is measured; hence, this skirt follows the phase noise of the LOs. The Doppler resolution Δf_d has to be considered, leading to a measured phase noise power of

$$P_{pn}(f_{offset})\big|_{dBc} = \Delta f_d \, \mathcal{L}(f_{offset})\big|_{\frac{dBc}{Hz}}. \tag{13}$$

Thus, the level of the velocity skirt is not only proportional to the LOs' phase noise power spectral density (PSD) $\mathcal{L}(f_{offset})$, but also to the Doppler resolution. The skirt hinders the detection of weaker targets in the same range cell as a stronger one.

Fig. 3 shows the simulations of a single target at 1 m with and without the phase noise shown in Fig. 4 (left). Comparing Fig. 3(a) and (b), both effects of phase noise are clearly visible. First, it increases the noise floor, resulting in a degradation of the PNR from 100 to 65 dB. The raised noise floor is also responsible for the noise increase in the range profile shown in Fig. 3(c) (right). Second, the expected Doppler domain skirt is visible in Fig. 3(b). This skirt equals the noise visible in the Doppler profile in Fig. 3(c) (left).

In Fig. 5, a measurement is shown. The scenario includes a strong RL and a single corner reflector at 4.3 m. Two measurements are compared, one with uncoupled LO sources, and one with a low-frequency coupling at 10 MHz. In both measurements, the DAC and ADC use the same reference frequency. In the uncoupled case, the Doppler profile is clearly affected by phase noise and a frequency offset. Due to the DSB mixer at the Rx, the frequency offset leads to two peaks. As expected, with a 10-MHz coupling, no frequency offset occurs. The phase noise is only partially mitigated since only the phase noise induced by the reference oscillator becomes correlated [48]. The PNR of the corner reflector is reduced by 4 dB in the uncoupled measurement compared to the coupled LOs. Yet this is not visible in the range profile due to the high sidelobes caused by nonidealities in the measurement system.
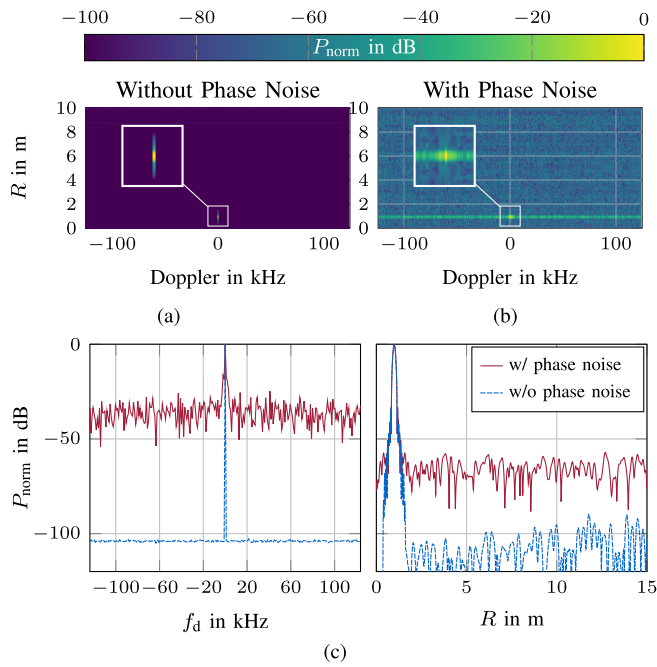
Fig. 3. Simulation of a single target at range $R = 1$ m. (a) Without phase noise. (b) With phase noise. (c) Doppler profile at the target and range profile at $v = 0$ m/s.
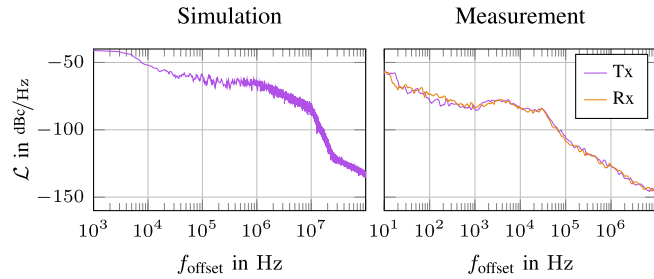
Fig. 4. Phase noise PSD as applied in simulations (left) and of the LO sources used in measurements (right).

D. Sample Frequency Offset

In the case of two uncoupled radar systems, not only the LO sources are uncoupled, but so are the clock sources used for the DAC and ADC. Assuming constant clock frequencies during a single frame, the uncoupled clock sources lead to an SFO. In the presence of an SFO, the sampled receive signal can be described as

$$\tilde{x}_{\mathrm{Rx}}[n] = x_{\mathrm{Rx}}(n(T_{\mathrm{s}} + \Delta T)) \tag{14}$$

where $n = 1, \ldots, T_{\mathrm{obs}}/T_{\mathrm{s}}$ is the sample index, T_{s} is the sampling period, T_{obs} is the observation time of a single frame, and $\Delta T = \delta \cdot T_{\mathrm{s}}$ is the timing offset caused by the SFO [49], [50]. This leads to the SFO, defined as the difference between the expected sampling frequency f_{s} and the true sample frequency $\tilde{f}_{\mathrm{s}}$ as

$$f_{\mathrm{SFO}} = f_{\mathrm{s}} - \tilde{f}_{\mathrm{s}} \overset{|\delta| \ll 1}{\approx} \delta f_{\mathrm{s}} \tag{15}$$

where the approximation takes into account the typically very small SFO, resulting in a very small relative clock error δ [50].
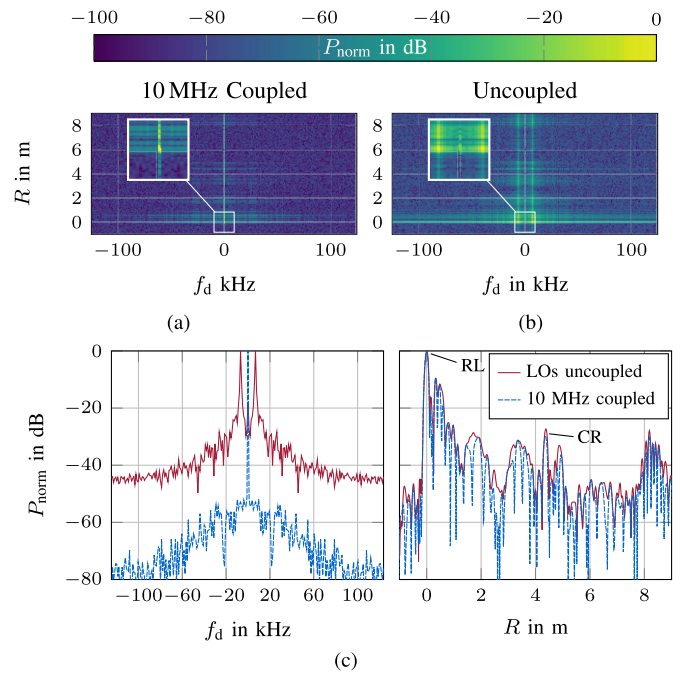
Fig. 5. Measurement of a corner reflector (CR) at $R = 4.3$ m. The DAC and ADC are coupled. (a) LOs low frequency coupled at 10 MHz. (b) LOs uncoupled. (c) Doppler profile at the RL and range profile at $v = 0$ m/s or, in the uncoupled case, at $v = v_{\mathrm{err}}$.

Inserting (4) and (7) into (14) leads to

$$\tilde{x}_{\mathrm{Rx}}[n] = \sum_{k=0}^{N_{\mathrm{T}}} a_{\mathrm{Rx},k} m(n(T_{\mathrm{s}} + \Delta T) - \tau_k) e^{j2\pi f_{\mathrm{d},k} n(T_{\mathrm{s}} + \Delta T)} e^{-j2\pi f_{\mathrm{Tx}} \tau_k}. \tag{16}$$

The error can now be considered for the range evaluation term $m(n(T_{\mathrm{s}} + \Delta T) - \tau_k)$ and the Doppler term $e^{j2\pi f_{\mathrm{d},k} n(T_{\mathrm{s}} + \Delta T)}$.

In the range evaluation, the cross-correlation is affected since the sampling of the received code sequence and the expected code sequence used for the correlation do not match. The range matrix $\mathbf{I}_{\mathrm{Range}} \in \mathbb{C}^{n_{\mathrm{b}} L_{\mathrm{c}} \times p}$, i.e., the matrix after the correlation as shown in Fig. 1 (center), equals

$$\mathbf{I}_{\mathrm{Range}}[n, p]$$
$$= \sum_{l=0}^{n_{\mathrm{b}} L_{\mathrm{c}} - 1} x_{\mathrm{Rx}}^*(l(T_{\mathrm{s}} + \Delta T) + p \, n_{\mathrm{b}} L_{\mathrm{c}}(T_{\mathrm{s}} + \Delta T)) m_0((l+n)T_{\mathrm{s}}) \tag{17}$$

where $(\cdot)^*$ denotes the complex conjugate. The SFO leads to two effects: the term $l(T_{\mathrm{s}} + \Delta T)$ describes the sampled time within a sequence p. Here, ΔT causes a smeared peak in every single range profile, with a peak width of $R_{\mathrm{smear, single \, RP}} = |n_{\mathrm{b}} L_{\mathrm{c}} \Delta T c_0/2|$. However, doing the full range-Doppler evaluation, this effect is neglectable. This is due to the term $p \, n_{\mathrm{b}} L_{\mathrm{c}}(T_{\mathrm{s}} + \Delta T)$, which describes the time frame moving from one transmitted sequence to the next, and its accumulated error due to ΔT. For every sequence p, this leads to a range offset $\Delta R_p = p \, n_{\mathrm{b}} L_{\mathrm{c}} \Delta T c_0/2$. Before Doppler processing, this creates a different range for every sequence. After Doppler processing, the range offsets of all correlations lead to a peak smeared to a width of

$$R_{\mathrm{smear, total}} = \left| N_{\mathrm{s}} n_{\mathrm{b}} L_{\mathrm{c}} \Delta T \frac{c_0}{2} \right|. \tag{18}$$

This article has been accepted for inclusion in a future issue of this journal. Content is final as presented, with the exception of pagination.

6

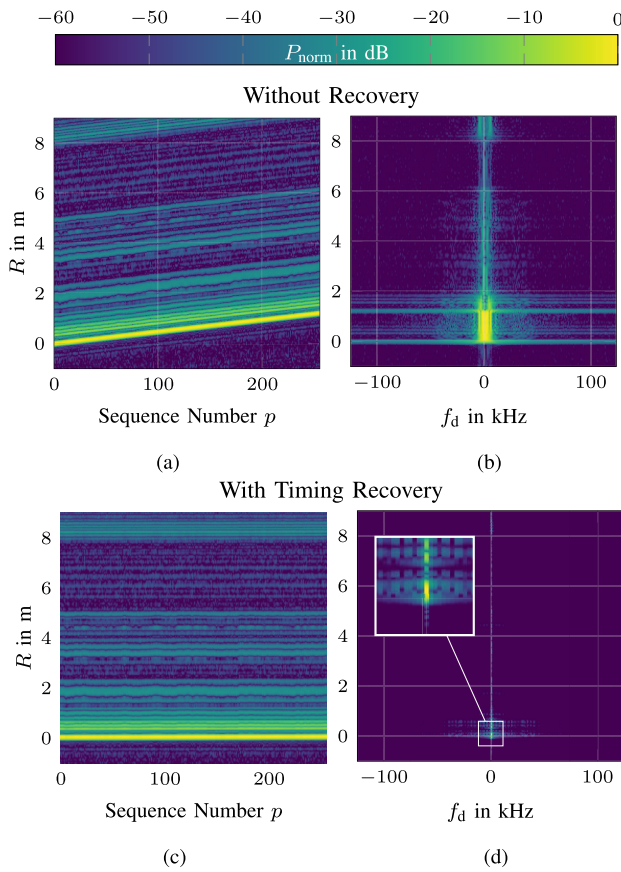IEEE TRANSACTIONS ON MICROWAVE THEORY AND TECHNIQUES

Fig. 6. Measurement of a corner reflector (CR) at $R = 4.3\,\text{m}$ with uncoupled DAC and ADC, but low-frequency coupled LOs. In (c) and (d), the evaluation is performed with timing recovery. (a) and (c) Range matrix after the cross-correlation. (b) and (d) Rv plot after the full signal evaluation.

This effect can be seen in Fig. 6: a measurement is shown, where the DAC and ADC are uncoupled, but the LOs are low-frequency-coupled. By this way, the measurement is mainly affected by the SFO, which is at about $78\,\text{kHz}$ in this case, resulting in $R_{\text{smear, total}} = 1.2\,\text{m}$. In Fig. 6(a), the range is increasing over the sequences leading to a broad peak in range direction in Fig. 6(b).

Due to the range ramp, each row in the range matrix before Doppler processing only has $N_{\text{s}}\Delta R / (R_{\text{smear, total}} + \Delta R)$ bins with signal power. Thus, each row's Doppler FFT is only based on these bins instead of a full row, leading to a broader Doppler peak and a Doppler resolution reduced to

$$\Delta \tilde{v} = \frac{R_{\text{smear, total}} + \Delta R}{\Delta R} \Delta v. \tag{19}$$

This effect is also noticeable in Fig. 6(b). Together, these effects lead to a large rectangular maximum per target instead of a single peak, making a proper target detection impossible.

Additionally, considering the Doppler shift of the kth target, the SFO leads to a miss-sampled Doppler term

$$\text{Doppler}_k[n] = e^{j2\pi f_{\text{d},k} n(T_{\text{s}} + \Delta T)} = e^{j2\pi f_{\text{d},k}(1+\delta)nT_{\text{s}}} \tag{20}$$

which equals a Doppler frequency offset of δf_D. This offset, however, is extremely small, especially compared to the effect described in (19), and thus can be neglected.

IV. TIMING RECOVERY

In Sections IV and V, correction methods are proposed. To begin with, a timing recovery is introduced, allowing to detect and correct the SFO. It is assumed that the SFO does not change significantly within a measurement frame.

A. Concept

The correct Tx sampling frequency is detected based on the square timing recovery presented in [23]. In the first step, a matched filter is applied by a convolution [denoted as $(*)$] with a single pulse $h[n]$. Then, the absolute value of the resulting signal $\tilde{x}_{\text{timing}}$ is squared, leading to

$$\tilde{x}_{\text{timing}}[n] = \left| \tilde{x}_{\text{Rx}}[n] * h[n] \right|^2 \tag{21}$$

which contains the true code repetition rate

$$\tilde{R}_{\text{c}} = \delta R_{\text{c}} \tag{22}$$

as spectral component [23]. This true code repetition rate $\tilde{R}_{\text{c}}$ includes the error due to the SFO. It is extracted by calculating $\tilde{X}_{\text{timing}}[k] = \text{FFT}(\tilde{x}_{\text{timing}}[n])$. Depending on the signal length, zero padding (ZP) must be applied to achieve a sufficient accuracy in the frequency estimation. Then, a defined frequency region around the expected R_{c} is extracted, and the frequency with maximum power in this region equals $\tilde{R}_{\text{c}}$. The true sampling frequency can now be calculated by

$$\tilde{f}_{\text{s}} = f_{\text{s}} \frac{\tilde{R}_{\text{c}}}{R_{\text{c}}} = n_{\text{b}} \tilde{R}_{\text{c}}. \tag{23}$$

After detecting the true sampling frequency, a Farrow filter-based resampling algorithm [51] is used to correct the sampling of the Rx signal to the expected sampling frequency f_{s}.

B. Verification

To evaluate the performance of the timing recovery, the same measurement presented in Fig. 6 is evaluated again, but with timing recovery and resampling to f_{s}. Fig. 7 shows $\tilde{X}_{\text{timing}}[k]$; $\tilde{R}_{\text{c}} = R_{\text{c}} - 7.8\,\text{kHz}$ can be extracted. Using (15) and (23), the SFO equals $78\,\text{kHz}$. Based on the $\tilde{f}_{\text{s}}$ estimated this way, a resampling is performed, changing the sampling frequency from $\tilde{f}_{\text{s}}$ back to f_{s}.

The results of a signal evaluation with timing recovery and resampling can be seen in Fig. 6(d). The shift in range over the sequences, visible in Fig. 6(a), is mitigated in Fig. 6(c). Thus, in the Rv plot in Fig. 6(d), the targets are nolonger represented by rectangles, but by sharp peaks, showing the good performance of the timing recovery.

V. CARRIER RECOVERY

In the next step, a digital carrier recovery is proposed to mitigate the phase noise and frequency offset caused by uncoupled LOs. This is possible by using a superheterodyne Rx with a digital intradyne down-conversion from IF. Hence, the signal is not downconverted to baseband in analog domain but to an IF-carrier, on which the signal is digitized. With the digital carrier recovery, the IF carrier is then recovered,
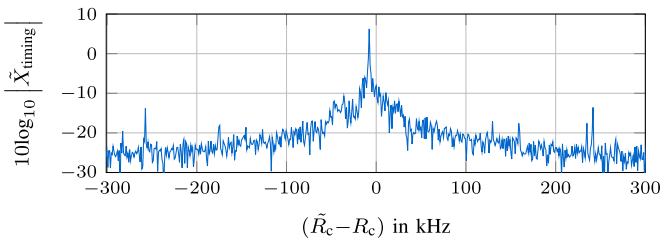
This article has been accepted for inclusion in a future issue of this journal. Content is final as presented, with the exception of pagination.

WERBUNAT et al.: ON SYNCHRONIZATION OF UNCOUPLED MULTISTATIC PMCW RADARS 7

Fig. 7. Spectrum of $\tilde{x}_{\text{timing}}[n]$. The x-axis shows the frequency offset of the recovered code rate $\tilde{R}_{\text{c}}$ compared to the expected code rate R_{c}.

including its phase noise and frequency offset. The recovered carrier is used for the digital IQ down-conversion of the receive signal, followed by a standard PMCW radar signal evaluation as described in Section II-D.

A. Carrier Recovery Concept

The concept of the proposed carrier recovery is shown in Fig. 8. It is based on two assumptions.

1) There is one path between the Tx–Rx pair, which leads to a much higher Rx power than all other paths. This path is referred to as RL (see Section II-B).
2) A BPSK-modulated radar signal is used, which is typical for PMCW radars.

After an analog down-conversion, the signal's IF carrier frequency equals

$$f_{\text{IF}} = f_{\text{Tx}} - f_{\text{Rx}} = f_{\text{IF,expected}} + f_{\text{cfo}} \tag{24}$$

including a frequency offset f_{cfo} of the expected IF carrier frequency $f_{\text{IF,expected}}$. Analogous to (10), the resulting carrier after an incoherent down-conversion to IF is given by

$$s_{\text{If}}(t) = e^{j2\pi f_{\text{IF}}t}e^{j\phi_{\text{n}}(t)}. \tag{25}$$

The target depended phase term $z_{\tau,k} = e^{-j2\pi f_{\text{Tx}}\tau_k}$ is not considered as part of the carrier but as part of the target response, and thus is excluded.

Based on (4), the IF receive signal can be described as

$$x_{\text{Rx,If}}(t) = \hat{x}_{\text{Rx,If}}(t) + n(t)$$
$$= \sum_{k=0}^{N_{\text{T}}} a_{\text{Rx},k}z_{\tau,k}m(t - \tau_k)e^{j2\pi f_{\text{d},k}t}s_{\text{If}}(t) + n(t) \tag{26}$$

where $k = 0$ denotes the RL. The signal $\hat{x}_{\text{Rx,If}}(t)$ is the noise-free IF signal used in the next steps for simplification.

The goal of the carrier recovery is to extract the carrier $s_{\text{If}}(t)$ out of $x_{\text{Rx,If}}(t)$ to allow for a coherent down-conversion with correlated phase noise. As shown in Fig. 8, this is done by several steps, starting with squaring to remove the BPSK modulation, followed by bandpass filters (BPs) and a frequency divider. Afterward, the recovered carrier is used for a coherent IQ downconversion. To do so, the complex carrier is calculated from the real-valued reconstructed carrier using a Hilbert transform. In the following, different steps of the carrier recovery are explained in detail, followed by a look at its different parameters and their influence on the performance.

B. Code Removal by Squaring

Assuming that the RL is much stronger than all other paths, i.e., $|a_{\text{Rx},0}| \gg |a_{\text{Rx},k}|\forall k \neq 0$, for the carrier recovery, (26) can be simplified to

$$\hat{x}_{\text{Rx,If}}(t) \approx a_{\text{Rx},0}z_{\tau,0}m(t - \tau_0)e^{j2\pi f_{\text{d},0}t}s_{\text{If}}(t). \tag{27}$$

Hence, squaring $\hat{x}_{\text{Rx,If}}(t)$ leads to

$$\hat{x}^2_{\text{Rx,If}}(t) \approx a^2_{\text{Rx},0}z^2_{\tau,0}\underbrace{\left(m(t - \tau_0)\right)^2}_{=1\text{ as }m(t)\in\{-1,1\}}e^{j4\pi f_{\text{d},0}t}s^2_{\text{If}}(t) \tag{28}$$

$$\overset{(25)}{=} a^2_{\text{Rx},0}e^{j2\pi(2f_{\text{IF}}+2f_{\text{d},0})t}e^{j(2\phi_{\text{n}}(t)-4\pi f_{\text{Tx}}\tau_0)} \tag{29}$$

$$= a^2_{\text{Rx},0}e^{j2\pi(2f_{\text{d},0}t-2f_{\text{Tx}}\tau_0)}s^2_{\text{If}}(t) \tag{30}$$

which includes the squared IF carrier containing f_{cfo} and the phase noise. Additionally, it contains a Doppler term and a phase offset due to the path between Tx and Rx. However, in a typical radar network scenario, the relative velocity between Tx and Rx is zero and, accordingly, the Doppler frequency of the RL equals $f_{\text{d},0} = 0\,\text{Hz}$.

Till now, the noise added by the channel was neglected for simplification. Considering it, (28) changes to

$$x^2_{\text{Rx,If}}(t) = \hat{x}^2_{\text{Rx,If}}(t) + 2\hat{x}_{\text{Rx,If}}(t)n(t) + n^2(t). \tag{31}$$

The carrier recovery is only possible if the signal-to-noise ratio (SNR) of $x_{\text{Rx,If}}(t)$ is high enough; hence, $|a_{\text{Rx},0}| \gg |n(t)|$. Therefore, the relevant noise term is $2\hat{x}_{\text{Rx,If}}(t)n(t)$, which leads to additional noise with a power proportional to the amplitude of the RL signal $a_{\text{Rx},0}$.

After squaring, a BP with a center frequency of $2f_{\text{IF,expected}}$ is used to extract the squared carrier $s^2_{\text{If}}(t)$. The filter's pass-band BW is crucial: if it is too low, parts of the phase noise will be suppressed resulting in partially uncorrelated phase noise. On the other hand, if it is too high, the recovered carrier is impacted by additional thermal noise and code residues.

C. Frequency Divider

In (30), the IF carrier is squared, and thus has the frequency $2f_{\text{IF}}$ and the doubled phase noise. In the next step, $s_{\text{If}}(t)$ is recovered by a frequency divider. In this work, a frequency divider using a square wave is implemented. At first, $x^2_{\text{Rx,If}}(t)$ is transformed into a square wave using a hysteresis. To sample the square wave at $2f_{\text{IF}}$ with a sufficient sampling frequency, the signal is upsampled within the carrier reconstruction. The upsampling factor must be chosen carefully as it has a significant impact on the computational costs. Then, the frequency is divided by extracting every second edge. Afterward, the higher harmonics leading to the square wave are suppressed by a BP. The result is a sine wave with frequency f_{IF}, which includes the phase noise and phase offset $\phi_{\text{n}}(t)$.

D. Parameterization and Performance

Several parameters massively influence the performance of the carrier recovery. In the following, these parameters are analyzed using simulations. If not stated otherwise, the carrier recovery parameters from Table II are used. The PMCW parameters equal the parameters from Table I, and the phase noise shown in Fig. 4 (left) is used.
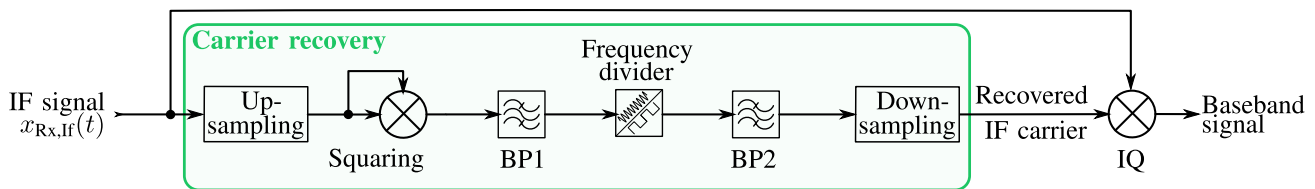
Fig. 8.   Concept of the carrier recovery.

TABLE II
CARRIER RECOVERY PARAMETERS

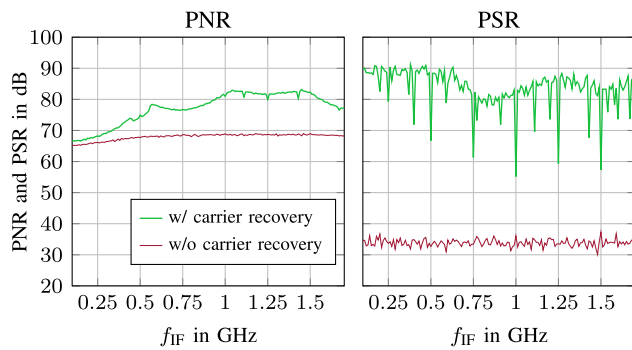|	Simulations	Measurements
IF frequency	$1.1 \cdot R_c = 1.1\,\mathrm{GHz}$	$1.1 \cdot R_c = 1.1\,\mathrm{GHz}$
Sample rate (upsampled)	$20\,\mathrm{GHz}$	$20\,\mathrm{GHz}$
BP1 center frequency	$2.2\,\mathrm{GHz}$	$2.2\,\mathrm{GHz}$
BP1 passband BW	$60\,\mathrm{MHz}$	$2\,\mathrm{MHz}$
BP2 center frequency	$1.1\,\mathrm{GHz}$	$1.1\,\mathrm{GHz}$
BP2 passband BW	$60\,\mathrm{MHz}$	$2\,\mathrm{MHz}$

Fig. 9.   PNR and PSR with and without carrier recovery for different IF carrier frequencies. Every data point is the mean value of ten simulations. PNR at the target referring to the ratio of peak power and noise floor (left). PSR referring to the ratio of peak power and velocity skirt (right).

1) IF Carrier Frequency: A proper IF carrier frequency f_{IF} is crucial for the carrier recovery performance. This can be seen in Fig. 9. Here, the performance of the carrier recovery is shown for different f_{IF} between $100\,\mathrm{MHz}$ and $1.7\,\mathrm{GHz}$. The simulated scenario includes one single target at a distance of $1\,\mathrm{m}$ representing the RL. To evaluate both effects induced by phase noise, the PNR and peak-to-skirt ratio (PSR) are used as performance measures. The PNR shown in Fig. 9 (left) is calculated as the ratio of the peak power to the mean power of the noise floor, as described in Section III-C. The PSR shown in Fig. 9 (right) refers to the velocity skirt. It is measured as the ratio of the peak power to the power of the maximum of the histogram of all velocity cells in the same range as the peak.

Considering the results of Fig. 9, the most important point is that the IF carrier frequency f_{IF} should not be a multiple of $R_c/4$. These frequencies appear as notches in Fig. 9 (right). The performance reduction is likely caused by strong code residues after the squaring of the signal. This is visible in Fig. 10, showing the spectrum of $x_{\mathrm{Rx,If}}^2(t)$ for $f_{\mathrm{IF}} = 1\,\mathrm{GHz}$ and $f_{\mathrm{IF}} = 1.1\,\mathrm{GHz}$. In the case of $f_{\mathrm{IF}} = R_c = 1\,\mathrm{GHz}$, the IF carrier has the same phase at the beginning of each code repetition, which leads to equal code residues in every repetition. Hence, strong residues are visible in Fig. 10 (left).
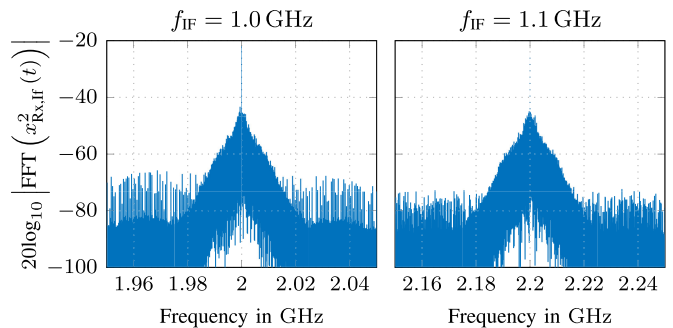
Fig. 10.   Spectrum of $x_{\mathrm{Rx,If}}^2(t)$ for different f_{IF}.

In contrast, in Fig. 10 (right), using $f_{\mathrm{IF}} = 1.1\,\mathrm{GHz} \neq R_c$, these residues are reduced.

To lower the ADC sampling rate, it is possible to use an $f_{\mathrm{IF}} < R_c$. As visible in Fig. 9 (left), this may lead to a reduction of the overall PNR. However, for $R_c/2 < f_{\mathrm{IF}} < R_c$, this reduction is small.

2) Filter BW: The purpose of the BP1 after squaring is to mitigate higher harmonics, code residues, and thermal noise. It should be chosen with a center frequency of $2f_{\mathrm{IF}}$ and a bandwidth (BW) large enough to include the relevant phase noise, as only the phase noise included in the recovered carrier is mitigated from the Rx signal in the IQ down-conversion. The second BP2 with a center frequency of f_{IF} is used to suppress the higher harmonics of the rectangular function, thus having relaxed BW requirements. It has to be considered that the filter design, especially its steepness, also significantly influences the computational costs.

In the simulations shown in this work, a filter BW of $60\,\mathrm{MHz}$ is chosen, including phase noise up to 30-MHz offset frequency and thus matching the relevant phase noise as visible in Fig. 4 (left). The phase noise of the signal source used in the measurement is depicted in Fig. 4 (right) and declines earlier; thus, for the measurements, the filter BW is reduced to $2\,\mathrm{MHz}$.

3) Reference Link: The first assumption of the carrier recovery concept is that the power of the RL exceeds the power of the sum of the other targets' signals and noise. To ensure a functioning carrier recovery, this condition must be met with a back-off of at least $6\,\mathrm{dB}$ [31, p. 226]. Considering the amplitudes of the signals received via the RL, $a_{\mathrm{Rx},0}$, and the targets, $a_{\mathrm{Rx},k}$, as well as the noise power P_{n}, this condition can be expressed as

$$|a_{\mathrm{Rx},0}| > 2 \left(\sum_{k=1}^{N_{\mathrm{T}}} |a_{\mathrm{Rx},k}| + \sqrt{P_{\mathrm{n}}} \right). \tag{32}$$

However, this condition assumes a worst-case scenario in which the signals of all N_{T} targets add up purely constructively. Depending on the scenario, the carrier recovery still

This article has been accepted for inclusion in a future issue of this journal. Content is final as presented, with the exception of pagination.

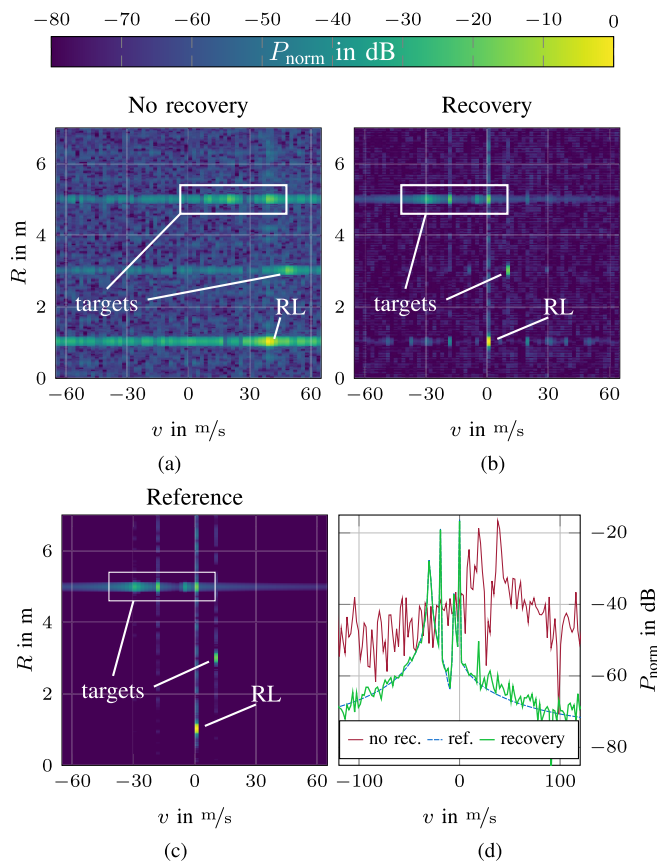WERBUNAT et al.: ON SYNCHRONIZATION OF UNCOUPLED MULTISTATIC PMCW RADARS

9

Fig. 11. Simulation of a multitarget scenario including an RL and five targets as stated in Table III. The simulation includes phase noise, but no LO frequency offset or SFO. (a) Without carrier recovery. (b) With carrier recovery. (c) Reference (ref.) without phase noise or CFO. (d) Velocity profile at $R = 5\,\mathrm{m}$.

TABLE III

MULTITARGET SCENARIO

Target	RL	1	2	3	4	5
R in m	1	3	5	5	5	5
v in m/s	0	9.5	0	-5.3	-19	-26.7
P_{norm} in dB	0	-16.9	-16.3	-37	-18.3	-27.6

works when (32) is violated, so it is a matter of reliability. The required $a_{\mathrm{Rx},0}$ can be calculated based on the targets' Rv peak powers $P_{\mathrm{peak},k} \propto |a_{\mathrm{Rx},k}^2|$, but it has to be considered that the peak's power may be spread over multiple Rv cells.

Yet a too high RL power also is disadvantageous. First, it leads to a loss in dynamic range due to sidelobes of the cross-correlation and the coupled noise term from (28). Second, the Rx hardware must be matched to the RL power to not drive its amplifier into saturation. In conclusion, a tradeoff must be made that takes into account the Rx hardware back-off, the power fluctuations of the RL and the targets, and the required reliability.

4) Multitarget Scenario: Using the derived parameters as presented in Table II, Fig. 11 shows the result of a scenario with multiple targets. The RL peak is 16.3 dB higher than the highest target peak. An overview over the RL and the five targets is given in Table III, including their peak power in Fig. 11(c). In this scenario, the RL power is recommended to exceed the power of the strongest target peak by approximately 16 dB according to (32).

Fig. 11(c) shows the error-free simulation result, where all targets are clearly detectable. With phase noise and frequency offset, in Fig. 11(a), they are affected by a velocity skirt, and the weakest target at $R = 5\,\mathrm{m}$ is not visible. This can also be seen in the velocity profile in Fig. 11(d). With the carrier recovery, in Fig. 11(b), these errors are mitigated. As visible in Fig. 11(d), the velocity profile now follows the reference. The PNR of the strong target at $R = 5\,\mathrm{m}$ and $v = 0\,\mathrm{m/s}$ equals 85 dB in the error-free case in Fig. 11(c). In Fig. 11(a), it is reduced to 49 dB due to the phase noise. In Fig. 11(b), it is increased back to 65 dB by means of the carrier recovery, showing the higher dynamic range accomplished.

E. Phase Reconstruction Performance

Depending on the use case, a correct elimination of the static phase offsets between the LOs is crucial. For example, this is the case for a network-based DoA estimation. As this static phase offset is part of $\phi_\mathrm{n}(t)$, it is mitigated by the carrier recovery leading to target phases independent of the LO phases. However, due to the carrier recovery, the phases measured at the targets' peaks still depend on the RL. Furthermore, due to the frequency divider, the target phases can only be estimated in a 180° unambiguous region. Thus, a calibration including the RL and a recovery method to overcome issues caused by the reduced unambiguous region may be necessary.

To validate the mitigation of the static LO phase offsets, simulations are performed. The same scenario as in Fig. 11 is used, and the phase of the static target at 5 m is evaluated. For a statistical evaluation, 1000 simulations with random static phase offsets, random frequency offset, and the phase noise from Fig. 4 (left) are performed. The frequency offsets are uniformly distributed between 0 and 20 kHz. After correcting the resulting phases to the unambiguous region of 180°, it is very constant with a mean value of 50.4° and a standard deviation of 0.3°.

VI. SYSTEM CONCEPT AND MEASUREMENTS

In the next step, both the carrier and the timing recovery are combined and validated using a 77-GHz measurement setup, adapting the radar system from Fig. 2 to be used with the recovery methods. Furthermore, a digital signal processing is proposed, combining the recovery steps explained in Sections IV and V.

A. Digital Signal Processing With Recovery Steps

The proposed digital signal processing with timing and carrier recovery is shown in the green box in Fig. 12. After digitizing the signal on the IF carrier, at first, the timing recovery explained in Section IV is performed. Then, the receive signal is resampled from the detected sample rate $\tilde{f}_\mathrm{s}$ to the correct sample rate f_s.

The next step includes the carrier recovery from Section V. The carrier is recovered and used to down-convert the resampled receive signal with an IQ downconverter. Afterward, the signal is filtered by an LP with a corner frequency of $2R_\mathrm{c}$, before the signal is evaluated using the standard PMCW signal processing from Section II-D.
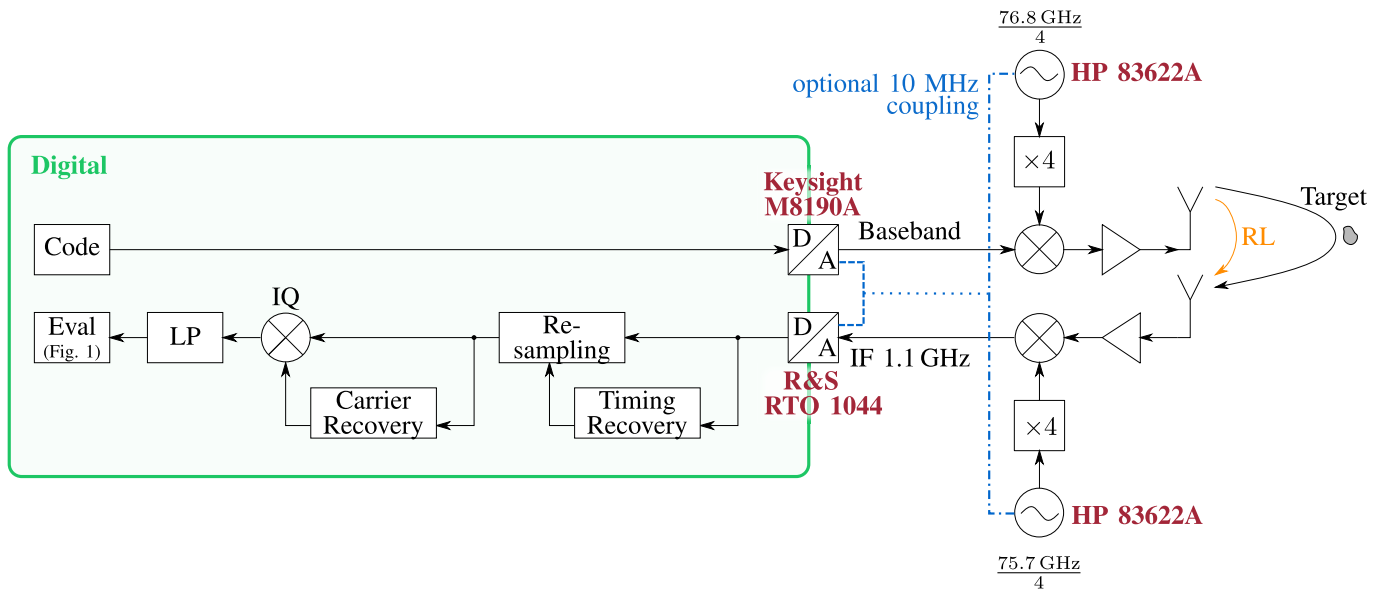
Fig. 12. PMCW radar and digital signal processing with timing recovery and carrier recovery.
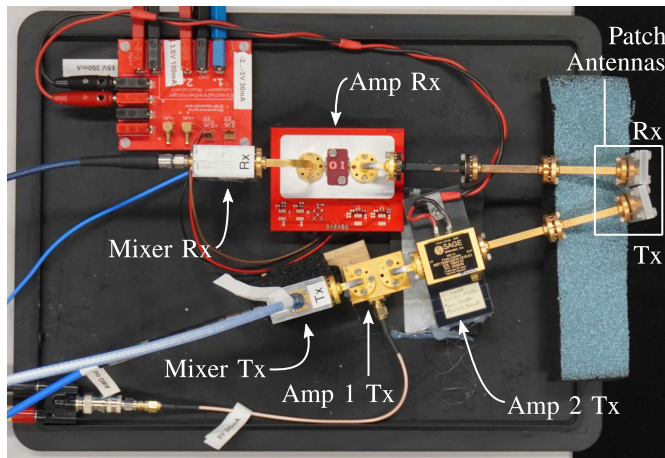
Fig. 13. Photograph of the RF part of the measurement system.

B. Measurements

A system consisting of a single Tx–Rx pair is used to validate the recovery methods, which is shown in Fig. 12. At Rx, an LO frequency 1.1 GHz lower (after the frequency multiplier) than the Tx LO frequency is used to downconvert the signal on the IF carrier. Fig. 13 shows a photograph of the RF part of the measurement system. As antennas, ten-element patch arrays from [52, Fig. 4] are used. They are placed closely together to ensure an RL strong enough. The measurements are performed in an anechoic chamber; as target, a corner reflector at a range of 4.3 m is used.

1) Carrier Recovery: Goal of the measurement shown in Fig. 14 is to validate the carrier recovery. Hence, the DAC and ADC are coupled, and the LOs are uncoupled. The evaluation without and with carrier recovery are shown in Fig. 14(a) and (b), respectively. For the evaluation without carrier recovery, instead of the recovered one, an ideal phase noise-free carrier at the expected IF carrier frequency of 1.1 GHz is applied. Without recovery, a velocity offset and skirt are visible. Both are corrected using the carrier recovery.
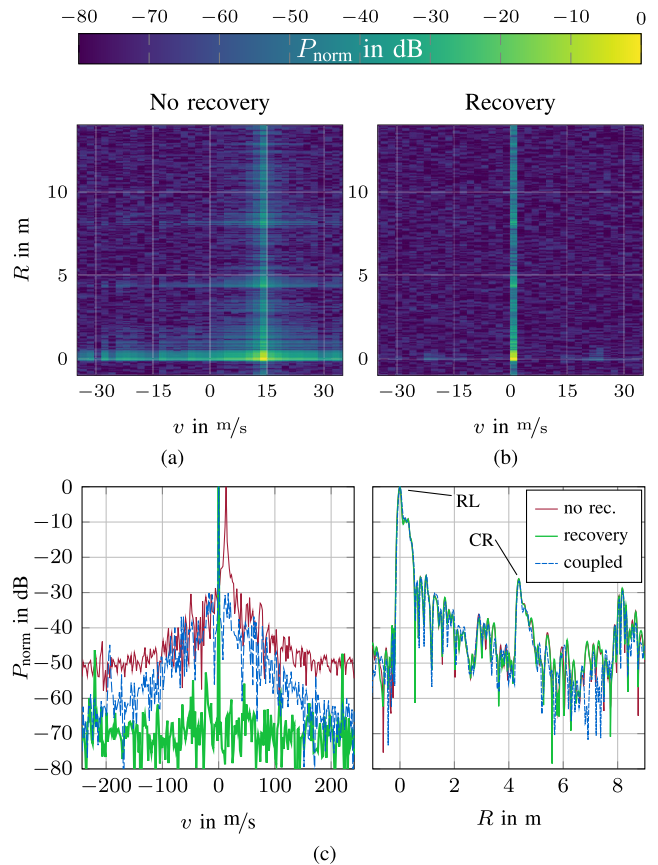
Fig. 14. Measurement using a setup with DAC and ADC coupled, but uncoupled LOs. The scenario includes the mutual coupling of the antennas as RL, and a corner reflector (CR) at 4.3 m. (a) Without carrier recovery. (b) With carrier recovery. (c) Velocity profile at the RL and range profile at $v = 0$ m/s or, without recovery, at $v = v_{\mathrm{err}}$.

In Fig. 14(c), the velocity skirt is nearly completely mitigated and shows a better performance than in the low-frequency coupled setup. However, the PNR does only differ by 2 dB between the three evaluations. This low effect on the PNR is similar to the measurement shown in Fig. 5 and could be due
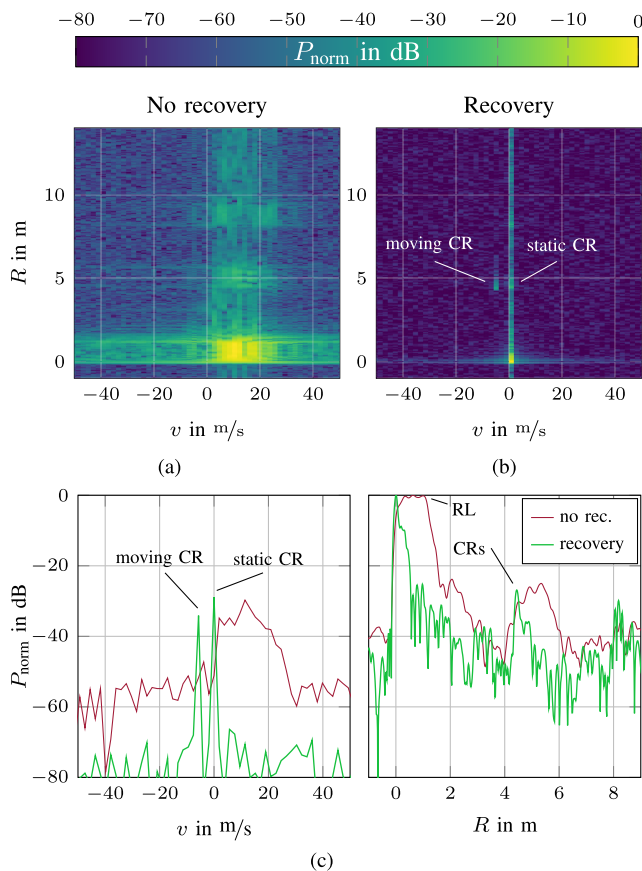
Fig. 15. Measurement using an uncoupled setup in an anechoic chamber. The scenario includes the mutual coupling of the antennas as RL, a corner reflector (CR) at 4.3 m, and a second CR is moved by hand at a similar R. (a) Without carrier and timing recovery. (b) With carrier and timing recovery. (c) Velocity profile at the targets ($R = 4.3$ m), and range profile at $v = 0$ m/s or, without recovery, at $v = v_{\mathrm{err}}$.

to the low-BW phase noise power spectral density (PSD) of the signal source.

2) Full Recovery: Fig. 15 depicts the measurement result of a completely uncoupled system, without recovery as well as with full timing and carrier recovery. Completely uncoupled means that there is no 10-MHz reference distribution between any of the measurement devices. Additionally to the static corner reflector, a second one moved by hand at approximately the same range is included into the scenario. Without recovery, in Fig. 15(a), no peak for a target or an RL is visible, as the effects due to the SFO, the CFO, and the phase noise affect the measurement. In Fig. 15(b), all those effects are corrected excellently, leading to sharp peaks for the targets and thus showing the high performance of the timing recovery and the carrier recovery.

VII. Conclusion

Without recovery methods, using uncoupled PMCW radars for multistatic measurements leads to a loss in performance due to phase noise, CFO, and SFO. With the methods proposed in this work, these effects are mitigated successfully. Using the timing recovery, sampling errors caused by the SFO are detected and then corrected by resampling the Rx signal. With the proposed carrier recovery, phase noise and CFO are corrected. Combining both, the presented measurements show

a very good performance, even exceeding the performance of a low-frequency coupled setup. Thus, the presented methods achieve a synchronized coherent signal evaluation just by digital signal processing at the Rx. By this way, they offer the possibility of coherent multistatic radar measurements and are promising for uncoupled radar network setups as well as for multistatic SAR applications.

References

[1] C. Waldschmidt, J. Hasch, and W. Menzel, "Automotive radar—From first efforts to future systems," *IEEE J. Microw.*, vol. 1, no. 1, pp. 135–148, Jan. 2021.

[2] P. Hügler, M. Geiger, and C. Waldschmidt, "Radar as an emerging and growing technology for industrial applications: A short overview," in *Proc. SENSOR*, May 2017, pp. 460–465.

[3] A. Grathwohl et al., "Taking a look beneath the surface: Multicopter UAV-based ground-penetrating imaging radars," *IEEE Microw. Mag.*, vol. 23, no. 10, pp. 32–46, Oct. 2022.

[4] B. P. Ginsburg et al., "A multimode 76-to-81 GHz automotive radar transceiver with autonomous monitoring," in *IEEE Int. Solid-State Circuits Conf. (ISSCC) Dig. Tech. Papers*, Feb. 2018, pp. 158–160.

[5] P. Ritter et al., "A fully integrated 78 GHz automotive radar system-an-chip in 22 nm FD-SOI CMOS," in *Proc. 17th Eur. Radar Conf. (EuRAD)*, Jan. 2021, pp. 57–60.

[6] B. Farley, J. McGrath, and C. Erdmann, "An all-programmable 16-nm RFSoC for digital-RF communications," *IEEE Micro*, vol. 38, no. 2, pp. 61–71, Mar. 2018.

[7] B. Schweizer et al., "The fairy tale of simple all-digital radars: How to deal with 100 Gbit/s of a digital millimeter-wave MIMO radar on an FPGA [application notes]," *IEEE Microw. Mag.*, vol. 22, no. 7, pp. 66–76, Jul. 2021.

[8] Z. Geng, "Evolution of netted radar systems," *IEEE Access*, vol. 8, pp. 124961–124977, 2020.

[9] M. Gottinger et al., "Coherent automotive radar networks: The next generation of radar-based imaging and mapping," *IEEE J. Microw.*, vol. 1, no. 1, pp. 149–163, Jan. 2021.

[10] G. Krieger and M. Younis, "Impact of oscillator noise in bistatic and multistatic SAR," *IEEE Geosci. Remote Sens. Lett.*, vol. 3, no. 3, pp. 424–428, Jul. 2006.

[11] G. Krieger and A. Moreira, "Spaceborne bi- and multistatic SAR: Potential and challenges," *IEE Proc.-Radar, Sonar Navigat.*, vol. 153, no. 3, pp. 184–198, Jun. 2006.

[12] A. Grathwohl, B. Meinecke, M. Widmann, J. Kanz, and C. Waldschmidt, "UAV-based bistatic SAR-imaging using a stationary repeater," *IEEE J. Microw.*, vol. 3, no. 2, pp. 625–634, Apr. 2023.

[13] D. Werbunat et al., "Multichannel repeater for coherent radar networks enabling high-resolution radar imaging," *IEEE Trans. Microw. Theory Techn.*, early access, Nov. 2023. [Online]. Available: https://ieeexplore.ieee.org/document/10335758

[14] A. Dürr, B. Schneele, D. Schwarz, and C. Waldschmidt, "Range-angle coupling and near-field effects of very large arrays in mm-wave imaging radars," *IEEE Trans. Microw. Theory Techn.*, vol. 69, no. 1, pp. 262–270, Jan. 2021.

[15] M. Gottinger, P. Gulden, and M. Vossiek, "Coherent signal processing for loosely coupled bistatic radar," *IEEE Trans. Aerosp. Electron. Syst.*, vol. 57, no. 3, pp. 1855–1871, Jun. 2021.

[16] M. Ash, M. Ritchie, K. Chetty, and P. V. Brennan, "A new multistatic FMCW radar architecture by over-the-air deramping," *IEEE Sensors J.*, vol. 15, no. 12, pp. 7045–7053, Dec. 2015.

[17] J. M. Merlo, S. R. Mghabghab, and J. A. Nanzer, "Wireless picosecond time synchronization for distributed antenna arrays," *IEEE Trans. Microw. Theory Techn.*, vol. 71, no. 4, pp. 1720–1731, Apr. 2023.

[18] A. Frischen, G. Hakobyan, and C. Waldschmidt, "Coherent measurements with MIMO radar networks of incoherent FMCW sensor nodes," *IEEE Microw. Wireless Compon. Lett.*, vol. 30, no. 7, pp. 721–724, Jul. 2020.

[19] A. Dürr, D. Böhm, D. Schwarz, S. Häfner, R. Thomä, and C. Waldschmidt, "Coherent measurements of a multistatic MIMO radar network with phase noise optimized non-coherent signal synthesis," *IEEE J. Microw.*, vol. 2, no. 2, pp. 239–252, Apr. 2022.

[20] U. Mengali, *Synchronization Techniques for Digital Receivers*. New York, NY, USA: Springer, Oct. 1997.

[21] M. Morelli, C.-C.-J. Kuo, and M.-O. Pun, "Synchronization techniques for orthogonal frequency division multiple access (OFDMA): A tutorial review," *Proc. IEEE*, vol. 95, no. 7, pp. 1394–1427, Jul. 2007.

[22] A. A. Nasir, S. Durrani, H. Mehrpouyan, S. D. Blostein, and R. A. Kennedy, "Timing and carrier synchronization in wireless communication systems: A survey and classification of research in the last 5 years," *EURASIP J. Wireless Commun. Netw.*, vol. 2016, no. 1, p. 180, Aug. 2016.

[23] M. Oerder and H. Meyr, "Digital filter and square timing recovery," *IEEE Trans. Commun.*, vol. COM-36, no. 5, pp. 605–612, May 1988.

[24] J. R. Barry, A. Kavcic, S. W. McLaughlin, A. Nayak, and W. Zeng, "Iterative timing recovery," *IEEE Signal Process. Mag.*, vol. 21, no. 1, pp. 89–102, Jan. 2004.

[25] C.-F. Wu, M.-T. Shiue, and C.-K. Wang, "Joint carrier synchronization and equalization algorithm for packet-based OFDM systems over the multipath fading channel," *IEEE Trans. Veh. Technol.*, vol. 59, no. 1, pp. 248–260, Jan. 2010.

[26] M. Morelli and U. Mengali, "A comparison of pilot-aided channel estimation methods for OFDM systems," *IEEE Trans. Signal Process.*, vol. 49, no. 12, pp. 3065–3073, Dec. 2001.

[27] M. Morelli and U. Mengali, "Carrier-frequency estimation for transmissions over selective channels," *IEEE Trans. Commun.*, vol. 48, no. 9, pp. 1580–1589, Sep. 2000.

[28] X. Wu, Y. Song, C. Zhao, and X. You, "Progressive frequency offset compensation in turbo receivers," *IEEE Trans. Wireless Commun.*, vol. 10, no. 2, pp. 702–709, Feb. 2011.

[29] E. Hosseini and E. Perrins, "Timing, carrier, and frame synchronization of burst-mode CPM," *IEEE Trans. Commun.*, vol. 61, no. 12, pp. 5125–5138, Dec. 2013.

[30] J. P. Costas, "Synchronous communications," *Proc. IRE*, vol. 44, no. 12, pp. 1713–1718, Dec. 1956.

[31] F. M. Gardner, *Phaselock Techniques*, 2nd ed. Hoboken, NJ, USA: Wiley, 1979.

[32] J. Layland, "An optimum squaring loop prefilter," *IEEE Trans. Commun. Technol.*, vol. COM-18, no. 5, pp. 695–697, Oct. 1970.

[33] C. Dick, F. Harris, and M. Rice, "FPGA implementation of carrier synchronization for QAM receivers," *J. VLSI Signal Process. Syst. Signal, Image Video Technol.*, vol. 36, no. 1, pp. 57–71, Jan. 2004.

[34] B. Purkayastha and K. Sarma, *A Digital Phase Locked Loop Based Signal and Symbol Recovery System for Wireless Channel*. New Delhi, India: Springer, Jan. 2015.

[35] J. Sachs, "M-sequence ultra-wideband-radar: State of development and applications," in *Proc. Int. Conf. Radar*, Sep. 2003, pp. 224–229.

[36] H. J. Ng, R. Feger, and A. Stelzer, "A fully-integrated 77-GHz UWB pseudo-random noise radar transceiver with a programmable sequence generator in SiGe technology," *IEEE Trans. Circuits Syst. I, Reg. Papers*, vol. 61, no. 8, pp. 2444–2455, Aug. 2014.

[37] V. Giannini et al., "A 79 GHz phase-modulated 4 GHz-BW CW radar transmitter in 28 nm CMOS," *IEEE J. Solid-State Circuits*, vol. 49, no. 12, pp. 2925–2937, Dec. 2014.

[38] K. E. Olsen et al., "Results from an experimental continuous wave low probability of intercept bistatic radar—The first steps toward multistatic radar," in *Proc. Int. Conf. Radar*, Sep. 2003, pp. 288–292.

[39] D. Mutz and K. George, "Costas loop and FFT based BPSK demodulation for pulsed radar receivers," in *Proc. IEEE Aerosp. Conf.*, Mar. 2016, pp. 1–12.

[40] H. Zhu, X. Shang, and J. Li, "Target parameter estimation via one-bit PMCW radar," in *Proc. IEEE Int. Conf. Acoust., Speech Signal Process. (ICASSP)*, May 2020, pp. 9145–9149.

[41] S. Stephany, B. Schweizer, C. Knill, and C. Waldschmidt, "Impact of an automotive chirp-sequence interferer on a wideband pseudo-noise radar," in *Proc. Int. Conf. Electromagn. Adv. Appl. (ICEAA)*, Sep. 2019, pp. 0859–0862.

[42] W. Lee, T. Dinc, and A. Valdes-Garcia, "Multi-mode 60-GHz radar transmitter SoC in 45-nm SOI CMOS," *IEEE J. Solid-State Circuits*, vol. 55, no. 5, pp. 1187–1198, May 2020.

[43] F. Probst, A. Engelmann, P. Hetterle, V. Issakov, R. Weigel, and M. Dietz, "A 15-Gb/s PMCW radar PRBS-generator for MIMO and joint radar-communication systems," in *Proc. Asia–Pacific Microw. Conf. (APMC)*, Nov. 2022, pp. 288–290.

[44] M. C. Budge and M. P. Burt, "Range correlation effects in radars," in *Proc. Rec. IEEE Nat. Radar Conf.*, Apr. 1993, pp. 212–216.

[45] W. Van Thillo, P. Gioffré, V. Giannini, D. Guermandi, S. Brebels, and A. Bourdoux, "Almost perfect auto-correlation sequences for binary phase-modulated continuous wave radar," in *Proc. Eur. Radar Conf.*, Oct. 2013, pp. 491–494.

[46] J. Overdevest, F. Jansen, F. Uysal, and A. Yarovoy, "Doppler influence on waveform orthogonality in 79 GHz MIMO phase-coded automotive radar," *IEEE Trans. Veh. Technol.*, vol. 69, no. 1, pp. 16–25, Jan. 2020.

[47] M. Bauduin and A. Bourdoux, "Impact of phase noise on FMCW and PMCW radars," in *Proc. IEEE Radar Conf. (RadarConf23)*, May 2023, pp. 1–6.

[48] A. Dürr et al., "High-resolution 160-GHz imaging MIMO radar using MMICs with on-chip frequency synthesizers," *IEEE Trans. Microw. Theory Techn.*, vol. 67, no. 9, pp. 3897–3907, Sep. 2019.

[49] L. Giroto de Oliveira et al., "Bistatic OFDM-based joint radar-communication: Synchronization, data communication and sensing," in *Proc. 20th Eur. Radar Conf. (EuRAD)*, Sep. 2023, pp. 359–362.

[50] L. Smaini, *RF Analog Impairments Modeling for Communication Systems Simulation: Application to OFDM-based Transceivers*. Wiley, 2012.

[51] T. Hentschel and G. Fettweis, "Continuous-time digital filters for sample-rate conversion in reconfigurable radio terminals," *Frequenz*, vol. 55, nos. 5–6, pp. 185–188, May 2001.

[52] C. Vasanelli, F. Bögelsack, and C. Waldschmidt, "Reducing the radar cross section of microstrip arrays using AMC structures for the vehicle integration of automotive radars," *IEEE Trans. Antennas Propag.*, vol. 66, no. 3, pp. 1456–1464, Mar. 2018.

David Werbunat (Graduate Student Member, IEEE) received the B.Sc. and M.Sc. degrees in electrical engineering from Ulm University, Ulm, Germany, in 2017 and 2019, respectively, where he is currently pursuing the Ph.D. degree at the Institute of Microwave Engineering.

His research interests include digital radar systems as well as system concepts, synchronization methods, and signal processing for uncoupled coherent radar networks.

Mr. Werbunat received the 2021 VDE ITG Prize for his outstanding work on orthogonal frequency-division multiplexing (OFDM)-based radar networks and the First Place in the IMS Advanced Practice Paper Competition in 2023.

Julian Aguilar (Graduate Student Member, IEEE) received the master's degree in electrical engineering from Ulm University, Ulm, Germany, in 2022, where he is currently pursuing the Ph.D. degree in electrical engineering at the Institute of Microwave Engineering.

His research interests include digital radar systems in the automotive sector and the accompanying signal processing.

Mohanid Almarashly received the B.Sc. and M.Sc. degrees in computer and communication engineering from Ulm University, Ulm, Germany, in 2019 and 2022, respectively. His master's thesis dealt with the construction of a coherent digital radar network based on a phase-modulated continuous wave (PMCW) radar at the Institute of Microwave Engineering, Ulm University.

Since 2022, he has been working as a Software Developer of mobile switchgear in mining trucks, Liebherr, Biberach, Germany.

This article has been accepted for inclusion in a future issue of this journal. Content is final as presented, with the exception of pagination.

WERBUNAT et al.: ON SYNCHRONIZATION OF UNCOUPLED MULTISTATIC PMCW RADARS
13

Vinzenz Janoudi (Graduate Student Member, IEEE) received the M.Sc. degree in electrical engineering from the University of Applied Sciences of Karlsruhe, Karlsruhe, Germany, in 2018, and the M.Eng. degree from Toronto Metropolitan University, Toronto, ON, Canada, in 2019. He is currently pursuing the Ph.D. degree in electrical engineering at the Institute of Microwave Engineering, Ulm University, Ulm, Germany.

From 2015 to 2016, he was a Bachelor Thesis Student and a Development Engineer with Rohde & Schwarz, Munich, Germany. In 2018, he joined Bosch Corporate Research, Renningen, Germany, as a Master Thesis Student of distributed source coding. From 2019 to 2020, he was a Development Engineer of signal intelligence receivers and direction finders with the PLATH Group, Hamburg, Germany. Since 2020, he has been a Research Assistant with Ulm University. His research interests include communication systems, system concepts for radar networks, and the accompanying signal processing.

Simon Stephany received the M.Sc. degree in electrical engineering from Ulm University, Ulm, Germany, in 2018.

He then joined the Institute of Microwave Engineering, Ulm University, as a Research Associate. In 2022, he founded a startup DeepSeek-Radar GmbH, Ulm, focusing on ground penetrating digital radar. His research interests include digital circuit design, hardware implementations of digital radars, and passive radar concepts.

Daniel Gil Gaviria (Graduate Student Member, IEEE) received the B.Sc. and M.Sc. degrees in electrical engineering and information technology from the Karlsruhe Institute of Technology (KIT), Karlsruhe, Germany, in 2018 and 2020, respectively, where he is currently pursuing the Ph.D. degree.

He is also a Research and Teaching Assistant with the Communications Engineering Laboratory (CEL), KIT. His research interests include modern multicarrier modulation schemes, joint communication and sensing (JCAS), and machine learning for communication.

Ahmet Çağrı Ulusoy (Member, IEEE) received the B.Sc. degree from Istanbul Technical University, Istanbul, Turkey, in 2006, the M.Sc. degree from Ulm University, Ulm, Germany, in 2008, and the Ph.D. degree from the Institute of Electron Devices and Circuits, Ulm University, in 2012, all in electrical engineering.

From 2012 to 2015, he was a Research Engineer with the Georgia Institute of Technology, Atlanta, GA, USA. From 2015 to 2016, he was the Team Leader of the Broadband Mixed-Signal ICs Group, IHP, Frankfurt (Oder), Germany. From 2016 to 2019, he was an Assistant Professor with Michigan State University, East Lansing, MI, USA. In January 2019, he became a Full Professor with the Karlsruhe Institute of Technology, Karlsruhe, Germany, and the Director of the Institute of Radio Frequency Engineering and Electronics. He has authored or coauthored over 150 publications in his research field. His research interests include the broad area of high-frequency integrated circuits and systems.

Dr. Ulusoy is a member of the Microwave Theory and Techniques Society and the Vice-Chair of the Technical Committee 14. He was a recipient and a co-recipient of several best paper awards. He served as the Technical Program Committee (TPC) Chair and the General Chair for the IEEE Topical Meeting on Silicon Monolithic Integrated Circuits in RF Systems and the TPC Chair for the IEEE International Conference on Microwaves for Intelligent Mobility. He served as an Associate Editor for IEEE MICROWAVE AND WIRELESS COMPONENTS LETTERS.

Christian Waldschmidt (Fellow, IEEE) received the Dipl.-Ing. (M.S.E.E.) and Dr.-Ing. (Ph.D.E.E.) degrees from University Karlsruhe (TH), Karlsruhe, Germany, in 2001 and 2004, respectively.

From 2001 to 2004, he was a Research Assistant with the Institut für Höchstfrequenztechnik and Elektronik (IHE), TH. Since 2004, he has been with Robert Bosch GmbH, Stuttgart, Germany, in the business units Corporate Research and Chassis Systems. He was heading different research and development teams in microwave engineering, RF sensing, and automotive radar. In 2013, he returned to academia. He was appointed as the Director of the Institute of Microwave Engineering, University Ulm, Ulm, Germany, where he is also a Full Professor. He has authored or coauthored over 300 scientific publications and holds more than 25 patents. His research topics focus on radar and RF sensing, millimeter-wave (mm-wave) and submillimeter-wave engineering, antennas and antenna arrays, and RF and array signal processing.

Dr. Waldschmidt is a member of the Executive Committee Board of the German MTT/AP Joint Chapter and the German Information Technology Society (ITG). He served as the Chair of the IEEE MTT-29 Technical Committee on Microwave Aerospace Systems and MTT-27 Technical Committee on Wireless Enabled Automotive and Vehicular Applications. He was a two-time TPC Chair and the General Chair of the IEEE MTT International Conference on Microwaves for Intelligent Mobility. In 2022, he was the General Chair of the German Microwave Conference. He was a three-time Guest Editor of *IEEE Microwave Magazine* and IEEE MICROWAVE AND WIRELESS COMPONENTS LETTERS (MWCL). From 2018 to 2022, he served as an Associate Editor for IEEE MWCL. He is a reviewer for multiple IEEE TRANSACTIONS and many IEEE conferences in the field of microwaves. He was co-recipient of more than 15 best paper awards. Since 2020, he has been a member of the Heidelberg Academy of Sciences and Humanities.